Defect Agglomeration and Electron Beam-Induced Local Phase Transformations in Single-Layer $MoTe_2$

Köster, J.; Ghorbani Asl, M.; Lehnert, T.; Komsa, H.-P.; Kretschmer, S.; Krasheninnikov, A.; Kaiser, U.;

Originally published:

June 2021

Journal of Physical Chemistry C 125(2021)24, 13601-13609

DOI: https://doi.org/10.1021/acs.jpcc.1c02202

Defect Agglomeration and Electron Beam-Induced Local Phase Transformations in Single-Layer $MoTe_2$

JANIS KÖSTER[1,*], MAHDI GHORBANI-ASL[2], HANNU-PEKKA KOMSA[3,4], TIBOR LEHNERT[1], SILVAN KRETSCHMER[2], ARKADY V. KRASHENINNIKOV[2,3] AND UTE KAISER[1,*]

[1] *Electron Microscopy Group of Materials Science, Ulm University, Albert-Einstein-Allee 11, 89081 Ulm, Germany*
[2] *Institut of Ion Beam Physics and Materials Research, Helmholtz-Zentrum Dresden-Rossendorf, 01328 Dresden, Germany*
[3] *Department of Applied Physics, Aalto University, PO Box 14100, 00076 Aalto, Finland*
[4] *Microelectronics Research Unit, University of Oulu, PO Box 8000, 90014 Oulu, Finland*
* *Corresponding Author: Janis Köster, janis.koester@uni-ulm.de; Ute Kaiser, ute.kaiser@uni-ulm.de*

***Abstract* – Atom migrations in single-layer 1H-$MoTe_2$ are studied with Cc/Cs-corrected high-resolution transmission electron microscopy (TEM) at an electron energy of 40 keV using the electron beam simultaneously for material modification and imaging. After creating tellurium vacancies and vacancy lines, we observe their migration pathways across the lattice. Furthermore, we analyze phase transformations from the 1H- to the 1T'-phase associated with the strain induced due to formation of Te vacancy lines. Combining the experimental data with the results of first-principles calculations, we explain energetics and driving forces of point and line defect migration and the phase transformations due to an interplay of electron-beam-induced energy input, atom ejection, and strain spread. Our results enhance the understanding of defect dynamics in 2D transition metal dichalcogenides, which should facilitate tailoring their local optical and electronic properties.**

I. Introduction:

Two-dimensional (2D) transition metal dichalcogenides (TMDs) with structural formula MX_2 consisting of a transition metal (M) atom sandwiched between chalcogen (X) atoms are novel materials, which have recently attracted lots of attention due to their tunable electronic characteristics ranging from insulators and semiconductors to metals[1]. Specifically, two-dimensional (2D) MX_2-TMDs offer new opportunities to develop electronic, spintronic, and optical devices[2,3,4,5,6,7].

Moreover, in contrast to the non-polymorphic 2D materials such as graphene[8–10,11] and single-layer hexagonal boron nitride[12], 2D TMDs can exist in different phases, which can be beneficial for

device engineering. 2D TMD can be synthesized as trigonal prismatic (H), octahedral (T), or monoclinic (T') phase structures[1,13]. 1H-TMDs have a hexagonal lattice with alternating metal and chalcogen atom columns, wherein the two chalcogen atoms are on top of each other. In the 1T-TMD phase, the chalcogen atoms of the first chalcogenide layer are located in the center of the hexagonal rings of the second layer. However, in group-VI chalcogenides, this phase should transform to the lower energy distorted 1T'-phase[1]. Transformations from the 1H to the 1T'-phase can be induced using several approaches, e.g., by electrostatic doping or atomic defect creation [14–16,17].

In this context, molybdenum ditelluride ($MoTe_2$) is one of the most interesting 2D TMDs as the energy difference between the semiconducting 1H and the metallic 1T'-phase is only ~ 31 meV per unit cell[18] and therefore, a phase transformation can easily be induced by heating[19], electrostatic gating[20]/doping[21] or adsorption of atoms[22]. Furthermore, using atomistic simulations Duerloo et al.[18] predicted that mechanical deformations can cause a switch between the semiconducting and the metallic phase in single-layer TMDs such as $MoTe_2$. Uniaxial tensile strains along the b axis (armchair direction) ranging from 0.3 to 3 % should transform $MoTe_2$ from 1H to 1T'-phase already at room temperature[18].

It was also reported that crystalline imperfections, such as vacancies, in 2D $MoTe_2$ can induce a phase transformation between the 1H and 1T' phases[20]. Due to the crucial impact on the characteristics of the 2D-based devices, defects in $MoTe_2$ monolayer and other 2D TMDs have extensively been studied. A substantial amount of knowledge on the behavior of intrinsic and extrinsic defects, such as vacancies or impurities, has been obtained[23–29]. Many insights came from the high-resolution transmission electron microscopy (HRTEM) experiments, which allow 'seeing' every atom in the 2D system and following defect structure evolution in real time. Besides, defects can deliberately be produced by the electron beam. In particular, the investigations for single-layer

$MoTe_2$ showed that point defects induced in one chalcogenide layer agglomerate mainly into single vacancy lines, while defects in both chalcogen layers are predominantly forming extended defects[29]. Defect-mediated transformations from the 1H into 1T′ phase, the formation of inversion domains with mirror twin boundaries, and complicated extended defects, which can be referred to as quantum dots, have been observed under electron irradiation[29,30].

Despite the previous research on defect behavior under electron beam in 2D $MoTe_2$, including our work[29], there are still many issues that have not yet been fully understood. Specifically, the open questions regarding the dynamics of extended defects are: (i) How do extended defects migrate and what elementary migration events are responsible for sliding and rotating single vacancy lines, forming inversion domains, and local transformations to the 1T'-phase? (ii) How external factors such as strain govern the evolution of complex defects? (iii) What are the energy barriers for these processes? (iv) Is it possible to induce these transformations in a controllable manner using electron irradiation in the TEM?

In this paper, which can be referred to as a follow-up work to our previous paper[29], we address the open issues listed above. We use chromatic (Cc) and spherical (Cs) aberration-corrected low-voltage HRTEM to study the *in-situ* formation of atomic defects and their dynamics in 1H-$MoTe_2$ induced by the electron beam, and we rationalize the results through density functional theory (DFT) calculations.

II. Methods section

Computational methods: Formation energies of defects and the structures were calculated with a plane wave basis Vienna ab initio simulation pack (VASP) code with a Perdew-Burke-Ernzerhof exchange-correlation functional (PBE) (REFs). The cut-off energy for plane wave basis was set at 600 eV for the primitive cell calculations. For supercells, we used 300 eV for the largest supercell consisting of a 10×10 unit-cell area. The Brillouin zones of the primitive cell and supercells were

sampled using a set of 14 × 14 × 1 and 4 × 4 × 1 k-points. In the optimized structures, the maximum force on each atom is less than 0.01 eV/Å. To avoid any artificial interaction between the layers and their images, a vacuum space of 20 Å was set along the direction perpendicular to the surface.

Sample preparation: Molybdenum ditelluride single-layers were mechanically exfoliated on a silicon dioxide substrate with a thickness of 90 nm. With an optical microscope, single-layers were identified due to contrast measurements and compared to calculations with the Fresnel formula[36–38], which yields a contrast of ~ 52 % for a single-layer of $MoTe_2$ on 90 nm SiO_2 illuminated with green light. After a single-layer was located, the flake was transferred to a Quantifoil TEM grid R 1.2/1.3 by bringing the grid in contact with the flake and the substrate by using a drop of isopropyl alcohol (IPA). Evaporation of the IPA and surface tension attached to the grid to the flake. With potassium hydroxide (KOH), the SiO_2 substrate was etched away and therefore releases the grid with the H-$MoTe_2$ flake. Afterward, the residues of the preparation are removed with double distilled water.

Experimental setup: The high-resolution TEM images were acquired at the Cc/Cs - corrected Sub - Ångström Low - Voltage Electron microscope (SALVE) at voltages of 40 kV. Measured values for Cc and Cs were in the range of -10 µm to -20 µm. The vacuum in the column of the TEM was in the range of 10^{-5} Pa.

III. Results and Discussions

Migration of single vacancy: To establish a link to the previously published HRTEM data on the behavior of isolated point defects in $MoTe_2$[29], we start analyzing defect diffusion by considering the migration of single vacancies and their agglomeration into extended defects.

Figs. 1 (a,b) show Cc/Cs-corrected 40 kV HRTEM images of freestanding 1H-$MoTe_2$. The honeycomb structure in Figs. 1 (a,b) is constructed by Mo atoms (indicated by turquoise dots in

the bottom left) and brighter Te_2 columns (indicated by orange dots). Red arrows mark a single vacancy (V_{1Te}). A V_{1Te} consists of single missing tellurium (Te) atom in a Te_2 column, which results in about half of the contrast compared to a Te_2 column. From Figs. 1 (a) to 1 (b), a migration step of a V_{1Te} within the same chalcogen layer is illustrated. Note that the vacancy diffusion is the motion of the neighboring Te atom. A second V_{1Te}, which was fixed in position during the recording time, is marked by a yellow dotted ring for better identification of the Te atom migration path. In the following, we have used this visual aid consistently for the 40 kV Cc/Cs-corrected HRTEM migration examples. Due to the atomic lattice symmetry, the three surrounding nearest neighbor Te atoms in the same chalcogen layer are equally likely to migrate and occupy the single vacancy.

In Fig. 1 (c), the calculated minimum energy pathways of the in-plane single vacancy migration (blue curve) and the single vacancy swap from one chalcogen layer to the other, which can also be referred to as migration perpendicular to the sheet (red curve), are shown. The pathway for the diffusion of an atom in the same side of the layer proceeds over a hexagon center to a nearest-neighbor single vacancy site. Here, the maximum energy barrier is about 1.6 eV, which is lower than the energy (4.87 eV) needed to displace one Te atom[29]. Moreover, the migration energy barrier is too high for thermal migration at room temperature, which indicates that the electron beam induces atom migrations[31]. In $MoTe_2$, the maximum kinetic energy transferred from 80 keV electrons to the nucleus is about 1.48 eV, which is in the energy range (cf. Fig. 1 (c)) needed to enable the V_{1Te} migration[31,32], especially when lattice vibrations are taken into account, resulting in initial kinetic energy of the atoms within the $MoTe_2$. At electron-beam energies of 40 keV, the maximum energy of 0.72 eV can be transferred, which should not be enough to break the intralayer covalent bonding between the metal and chalcogenide atoms, even with lattice vibrations. However, it was shown that electronic excitations in general[33] and specifically a combination of

inelastic scattering mechanisms could reduce the threshold energies so that atom removal and migrations below the 'ground state' energy barriers can be induced[34]. In addition, the occurrence of further defects in the nearby neighborhood of a vacancy can lower the energy barrier[35].

The kinetic pathway barrier of atom swapping (cf. red curve in Fig. 1 (c)) is similar in height than the sliding of a single Te atom to occupy a single vacancy. We assume that 'swapping' of single atoms in single vacancy lines occurs less likely than migrations of atoms on one side of the single-layer. This assumtion can be attributed to the fact that vacancies in both chalcogenide sides of the single-layer agglomerate to extended defects composed of column Te vacancies, including rotational trefoil-like defects[29].

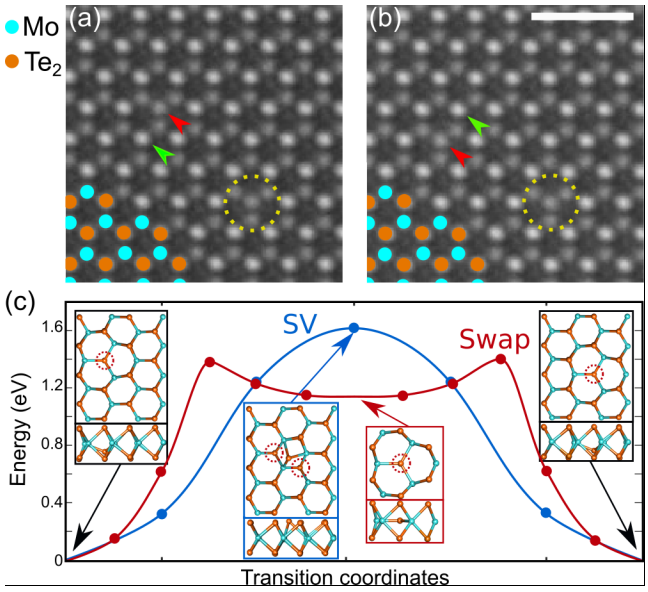

Figure 1: 40 kV Cc/Cs-corrected HRTEM images of freestanding single-layer $MoTe_2$ with bright atom contrast are shown in (a) and (b). A migration step of a single Te vacancy in single-layer $MoTe_2$ can be seen from (a) to (b). For better visualization, the vacancy is marked with a red arrow, and the green arrow marks the involved Te atom, which moves into the former vacancy position. The yellow dotted rings mark a V_{1Te}, which did not move during the experiment and can be used as a fixed point to follow the migration. The scale bar is 1 nm. In (c), a diagram shows the calculated minimum energy pathways of the in-plane single vacancy migration (blue) and the single vacancy swap from one chalcogen layer to the other (red). Atomic structures from selected steps are also indicated. The red dotted circles mark the positions of a Te single vacancy.

2-vacancy line sliding and rotation: Fig. 2 shows a 40 kV Cc/Cs-corrected HRTEM images of V_{1Te}, which is rotating from (a) to (b) around another V_{1Te}, which together form the shortest possible vacancy line. Red arrows mark the vacancy lines constructed of single Te vacancies in all the following HRTEM images. The vacancy line can be rotated by multiples of 60 degrees, with the orientation along any of the zigzag directions of the hexagonal lattice structure in 1H-$MoTe_2$ single-layer. However, the clockwise- and anticlockwise rotations will traverse through different atomic environments (a Mo atom on one side of the vacancy line and a hexagon center on the other), which yields in different migration barriers. The structure shown in Fig. 2 (c) illustrates the two main migration paths and the diagram in Fig. 2 (d) presents the corresponding calculated energy pathways of the two possible atom migrations. In both paths, the Te atom migrates via the center of the hexagonal ring, where it is surrounded by zero Te atoms in path-1 and one Te atom in path-2, as was also discussed earlier for MoS_2[31]. The path-1 transition state configuration appears locally similar to the 1T-phase, which in $MoTe_2$ is energetically very close to the 1H-phase, while the path-2 transition state configuration experiences "repulsion" from the neighboring Te atoms. Indeed, as evident from the calculated barriers presented in Fig. 2 (d), path-1 should be more probable than path-2. Path-1 consists of three steps: First, the energy of ~0.15 eV is required to break bonds and force the atom into the intermediate state, where the atom rests in the center of a hexagon. Second, a maximum energy barrier of ~0.18 eV needs to be exceeded to rotate the local bonding motif, which experiences symmetry breaking due to Jahn-Teller distortion. In the last step, a ~0.07 eV barrier follows for the Te atom to return from the center of the hexagon to the normal Te site. Since atomic reactions take place in the range of femtoseconds and exposure times in the range of seconds are necessary to reach an interpretable signal-to-noise ratio, the individual steps of the migration cannot be captured. As an example, we have shown in Figs. 2 (a) to 2 (b) the time period of 3s.

These two directions of motion (path-1 and path-2) are fundamental for explaining other movements of line defects. This is clearly shown by the second example in Figs. 2 (e,f), in which the sliding of an equally long vacancy line (V_{2Te}) to a neighboring lattice position is demonstrated. The calculated migration path (not shown) indicates that the sliding occurs via sequential path-1 and path-2 events (i.e., two sequential rotations) instead of concerted movement. To mark the two-step process, arrows in the pathway colors (orange for path-1 and light blue for path-2) are inserted in (e). The direction of motion in this example suggests that to keep the two vacancies in the nearest-neighbor sites, a path-1 event must occur first, followed by a path-2 event.

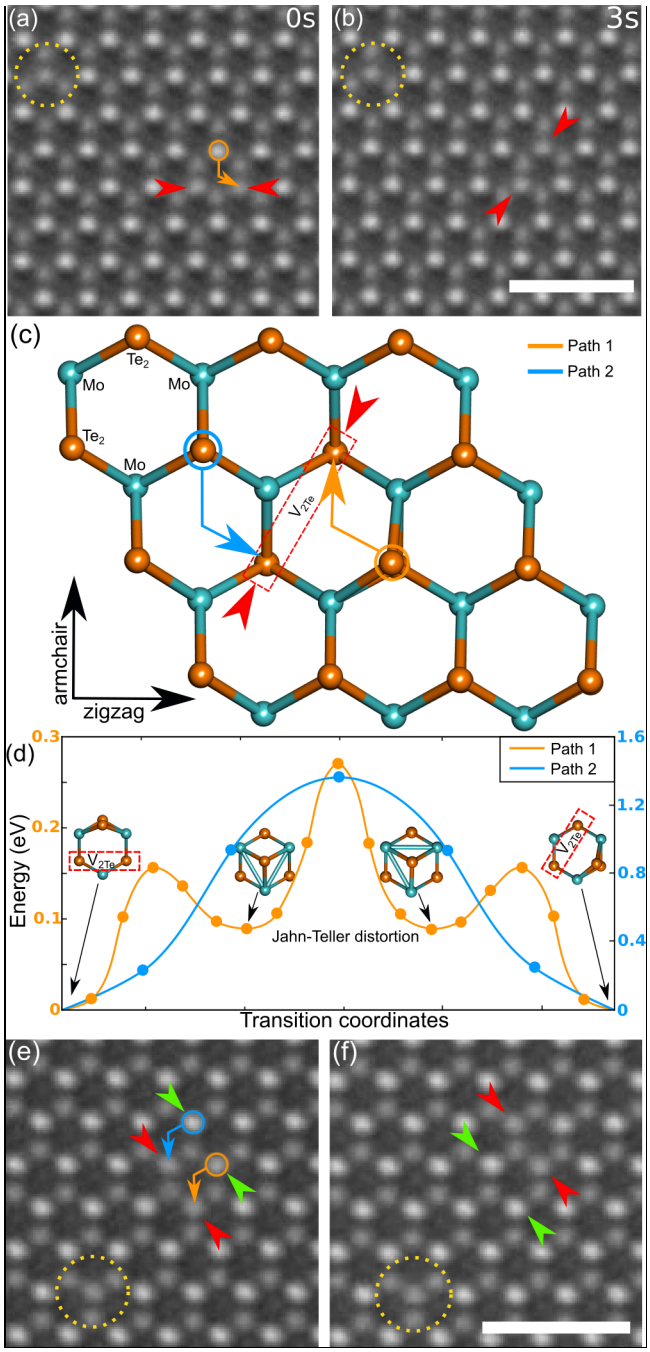

Figure 2: 40 kV Cc/Cs-corrected HRTEM images of $MoTe_2$ with a short Te vacancy line (marked by red arrows), consisting of two single vacancies, is shown in (a). (b) After 3 seconds, the vacancy line performs a 60° rotation. (c) Illustration of the two paths leading to vacancy line rotation: Path-1 (orange) is the energy landscape for migration via the center of a hexagon shown in the corresponding structure simulations in orange. Path-2 (light blue) shows the energy pathway via a Mo site. The corresponding energy pathways are shown in (d), and the local bonding changes for the energy minima along path-1. In addition, (e) and (f) show a sliding vacancy line which shows that both the

path-1 and path-2 events must occur to enable the sliding. Colored arrows in (e) mark the two events. The scale bars are 1 nm.

4-vacancy line sliding and rotation: That same consideration can also be used to understand the migration of longer vacancy lines through the lattice, as illustrated in Fig. 3. Structure models in Fig. 3 (a) show the individual steps during the sliding of a single vacancy line with four missing Te atoms (V_{4Te}). Single vacancies are marked with red dotted rings. Colored arrows show the direction of movement of the involved atoms to fill the marked vacancies. Orange arrows describe the movement of an atom through the lattice with a path-1 event and light blue arrows a path-2 event. The position of the Te vacancy line during the movement is marked with red arrows in the starting and final structure models. To move the entire line through the lattice, four individual events must be carried out. Figs. 3 (b, c) show the corresponding 40 kV Cc/Cs-corrected HRTEM images of vacancy lines with four missing Te atoms. With respect to the yellow marked point defect, the vacancy line slides diagonal through the lattice from (b) to (c). In the zigzag direction, the distance corresponds to 3.5 Å and along the projection in armchair direction to 3 Å. Fig. 3 (d) shows the calculated energy pathway of the sliding vacancy line for the steps shown in Fig. 3 (a). The three path-1 steps (I-III) have a small barrier, as in the case of V_{2Te} and thus expected to proceed fast, whereas the last path-2 step has a fairly high barrier. Even though four Te atoms are involved in the sliding process, the maximum energy barrier (~1.5 eV) is even lower than for the V_{1Te} migration (~1.6 eV, see Fig. 1 (c)). Due to the hexagonal symmetry of the atomic lattice, the single vacancy line can also slide in the opposite direction. However, in this case, the order of migration steps is inverted: first one path-2 step and then three path-1 steps.

Figs. 3 (e) to 3 (g) show an example for the rotation of a single vacancy line consisting of V_{4Te}. In our experiments, the rotation of single Te vacancy lines formed by up to 5 vacancies was observed. For a rotation of a V_{4Te} line, our DFT calculations resulted in two different possible migration

processes. First, the rotation can be achieved by a step-by-step execution event, similar to the process shown in Fig. 3 (a) but consisting of only small barrier path-1 events. Or secondly that all involved atoms move into a hexagonal center in the structure so that a triangular 1T-phase is formed (cf. inset in Fig. 3 (g)), from which the atoms can reorient themselves and rotate the vacancy line. The energy pathways for the two exemplified migration processes in Fig. 3 (g) indicate that, while the triangular 1T-phase has low energy, the migration barriers to that configuration are much higher than for the path-1 events. The rotation occurs very fast, and no fully developed triangular intermediate state (like shown in Fig. 3 (g), middle inset), where the tellurium atoms are located in the center of the hexagons, could be imaged experimentally. This supports the notion that the rotation process proceeds via sequential path-1 events. We do not observe the intermediate states due to these path-1 events either. We expect that these events occur very fast, one after another, but after most of these attempts, the system returns to the original vacancy line configuration.

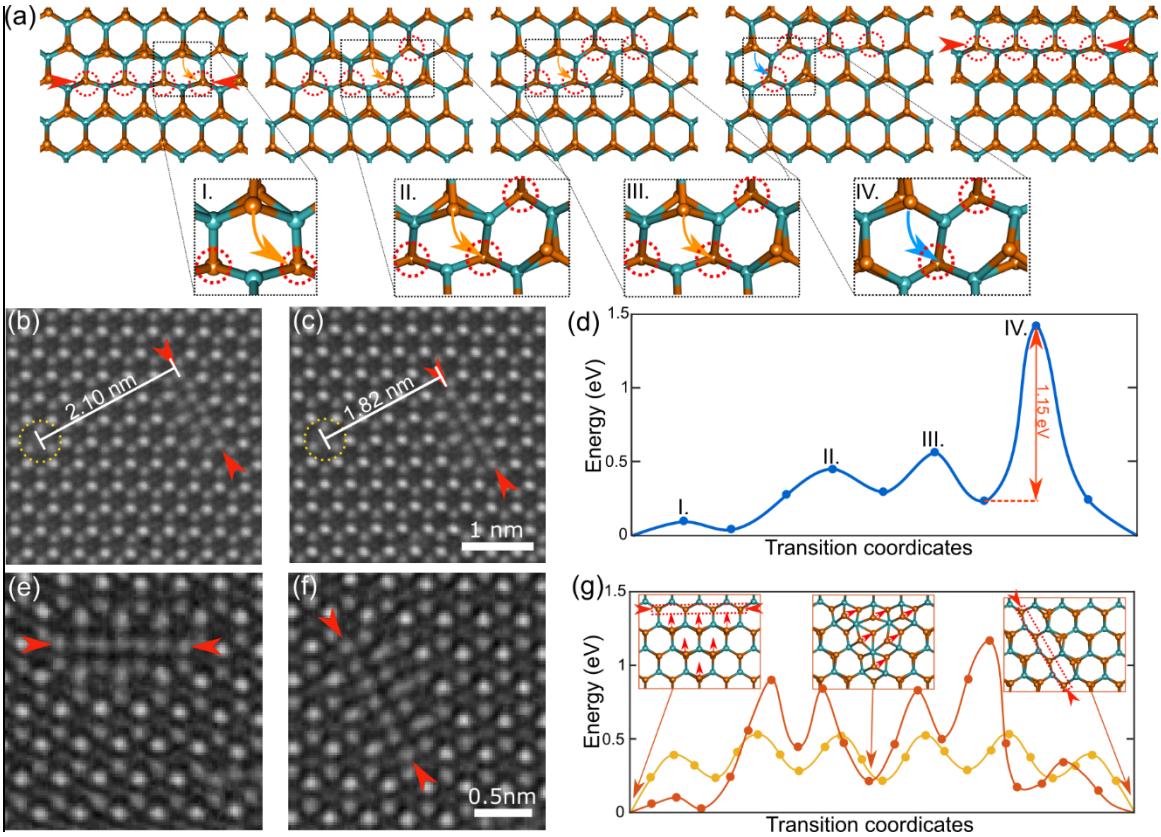

Figure 3: (a) Illustration of the step-by-step migration of a single vacancy line. The single vacancies are marked by red dotted rings and the corresponding line defect by red arrows. Enlarged regions highlight the single migration events, at which orange arrows describe a path-1 event and light blue arrows a path-2 event. Cc/Cs-corrected 40 kV HRTEM images of a sliding V_{4Te} is shown in (b,c) and the corresponding energy landscape in (d). For the measure V_{4Te} movement, we use a fixed-point defect (yellow circle). The vacancy line moves about 0.3 nm towards the point defect. In (e) and (f) a rotation process is displayed. (g) shows the corresponding energy landscapes for the rotation via a triangular T-phase structure in orange (also displayed by the insets) and via several path-1 events in yellow.

We occasionally observed relatively stable 1T'-phase islands, as shown in Fig. 4, where a single Te vacancy line transforms to a trapezoidal 1T'-phase region. To clarify the positions of the atoms, an overlay of the structures in (a) and (b) has been inserted, as shown in the corresponding panels below. The structure of the 1T'-phase is similar to that shown in Fig. 3 (g). Also, Fig. 3 (f) shows that transforming it back to the vacancy line requires overcoming relatively large barriers according to their observed stability.

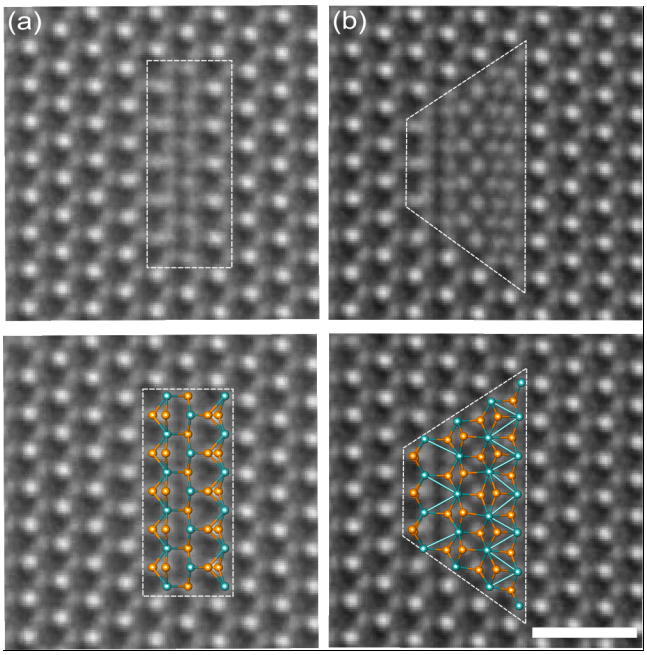

Figure 4: Phase transformation in 1H-$MoTe_2$ to the 1T'- phase over a width of two-unit cells. The initial structure in the 1H-phase in (a) is a single-vacancy line with a length of six missing Te (V_{6Te}) atoms. (b) shows the local trapezoidal 1T'-phase. Structure simulations are added in the lower panels to mark the atom position. The scale bar is 1 nm.

Strain analysis of different line defects: To understand the driving force for the observed transformations, we investigate the development of strain around line defects and the effect of the strain of defect energetics. We note that the 'straintronics' is a widely used approach to tailor the properties of 2D materials and the heterostructures, for an overview, see, e.g., K S Novoselov and A H Castro Neto, Phys. Scr. T146 (2012) 014006]. There is, however, a fundamental difference between the 'standard' approach where strain is created externally, by using, e.g. AFM cantilever, and the situation in our experiment, where strain naturally comes from the point and line defects created by the electron beam.

We found that locally induced lattice distortions nearby a single Te vacancy line strongly depend on their length, as shown in Fig. 5 (a). The distortion dependence due to strain perpendicular to the vacancy line results in a shift of the neighboring Te atoms to no longer be arranged in a column.

Lattice strain was measured in the line scan between the signal of the Te_2 columns in the pristine lattice (red dashed lines) and the shift of the corresponding Te_2 columns due to the vacancy lines indicated by the black arrows. The lattice strain was estimated to be 1.9 % for a V_{2Te} line and goes up to 7.2 – 7.4 % for vacancy lines with 4 or 6 missing Te atoms. In the V_{2Te} line example, a shift between the two nearest neighbor Te_2 atom rows is not visible in the HRTEM image but in the line scan where the third Te_2 peak from the left is slightly shifted from the red dashed line (indicated by the black arrow). For the V_{4Te} line, the intensity peaks between the Mo and Te_2 column are not distinguishable anymore because the two Te atoms are strongly shifted apart from each other, resulting in a broadened peak in the intensity profiles for the second Te_2 column from the left. The same effect can be seen for the V_{6Te} line.

DFT-based optimized structures of an infinite single Te vacancy line in the top and side view are depicted in Fig. 5 (b). To distinguish between long- and short-range strain fields at an infinite single Te vacancy line, we performed DFT strain simulations shown in (c). The calculated strain map indicates the induced lattice strain by colors, where red area represents expansion and blue stands for compression. The maximum lattice expension and compression within the structure are of the order of 3 %. The overall strain caused by such an infinite single vacancy line induces a lattice distortion of 8 %, which is very close to the experimentally obtained values for the listed V_{4Te} and V_{6Te} single vacancy lines in Fig. 5 (a). The maximal lattice distortion of 8 % can be appreciated in the side view of the infinite single vacancy line in Fig. 5 (b).

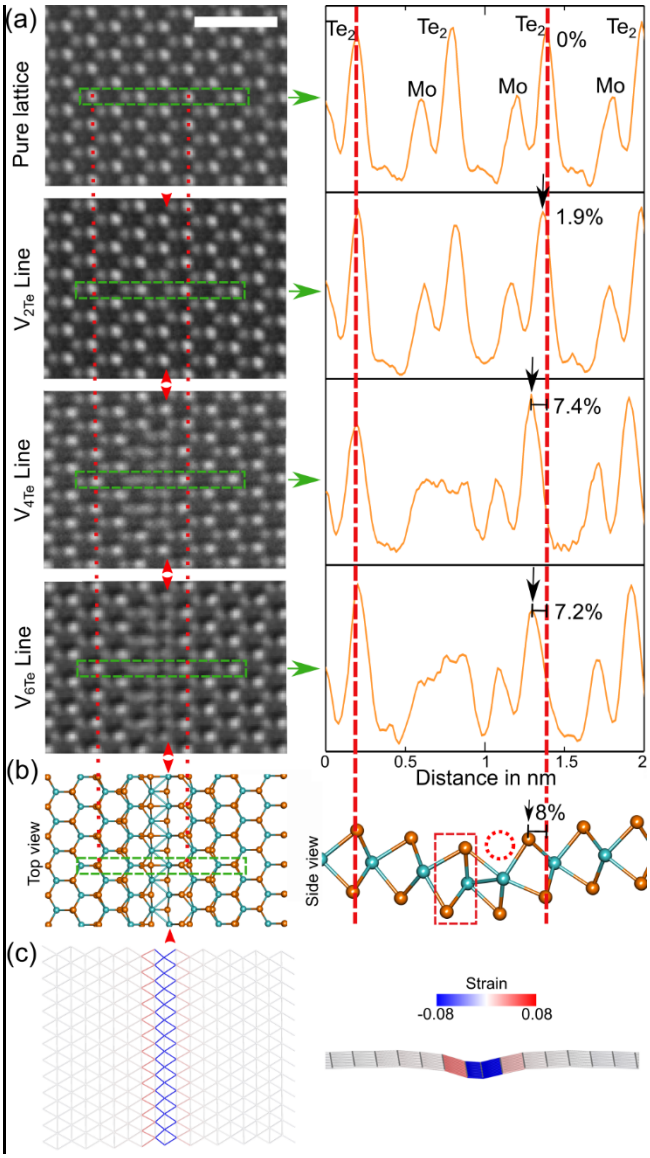

Figure 5: 40 kV Cc/Cs-corrected TEM images of 1H-$MoTe_2$ showing, from top to bottom, pure lattice, different single Te vacancy lines with V_{2Te}, V_{4Te}, and V_{6Te}. The location of the vacancy lines is indicated by the red arrows. Corresponding line profiles taken within the green dashed frames are given in the right panel of (a). The scale bar is 1 nm. The line profiles are showing distortion of the two Te atoms close to the line defect, which can be determined by the shift of the Te_2 peak (black arrows) due to the vacancy line compared to the Te_2 peaks of the pure lattice (red dashed lines). A distortion in the lattice rises with the increasing length of the vacancy lines up to ~7 % for a line consisting of four or more vacancies. For better identification, DFT-relaxed structure simulations of an infinite single Te vacancy line are shown in (b). The side view shows the distortion of the nearby Te_2 column in the red dotted box. A strain map showing the local strain effect of the in (b) shown infinite single vacancy line is depicted in (c).

4-vacancy line strain-dependent rotation: Since vacancies produced under the electron beam lead to local lattice contraction, this will lead to tensile strain in other parts of the sample. The magnitude

and direction of the strain depend on the concentration and positions of the defects and will thus evolve over time. The driving force for vacancy line rotation is likely the strain-induced after defect creation. Figs. 6 (a,b) illustrates the effect of uniaxial strain on a single V_{4Te} line, where

$$\Delta E_f = E_f(\theta = 0°) - E_f(\theta = 60°)$$

is the difference in formation energy E_f for different orientations θ of the single vacancy line. DFT simulations showed that the rotation of a vacancy line of 60 degrees becomes energetically favorable by applying strain perpendicular to the vacancy line. Fig. 6 (a) compares the effects of strain parallel (uniaxial – x, blue), perpendicular (uniaxial – y, red) to the line defect, and that for the biaxial strain (black) to the line defect. The uniaxial-y strain is favored compared to the biaxial and the uniaxial-x strain, which can even lead to an energy gain. In total, the larger the occurring strain in the uniaxial-y direction, the more energetically favorable the rotation becomes.

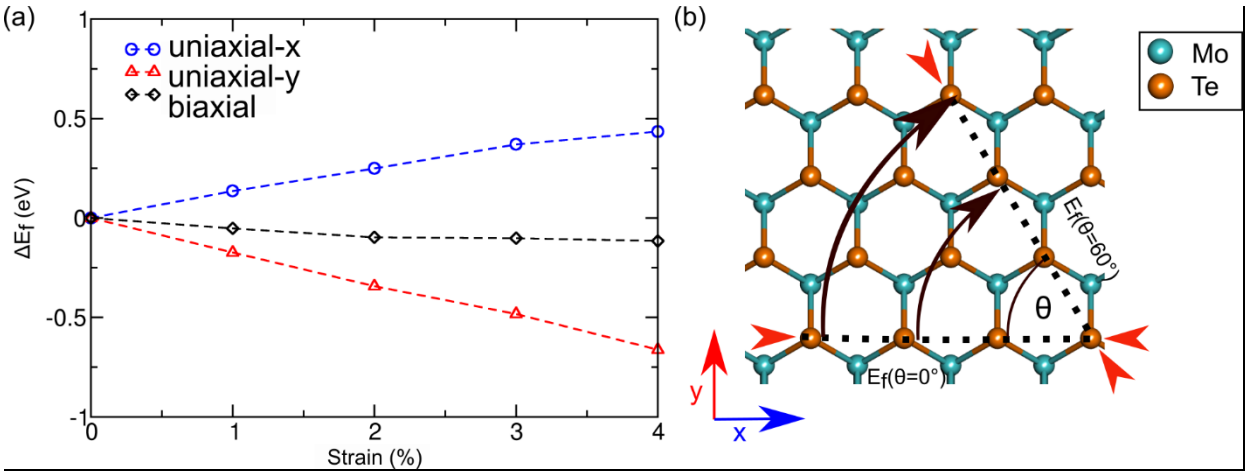

Figure 6: (a) Formation energies of line defects as functions of direction-dependent strain, which show a striking change with increasing strain. (b) Schematic illustration of the rotation process, which indicates the x- and y-directions. The blue curve in (a) represents the case of uniaxial-x strain (parallel) and the red curve uniaxial-y strain (perpendicular) to the vacancy line. Strain perpendicular to the initial vacancy line orientation gives rise to energy gain. Biaxial strain (black curve) favors no orientation.

Formation energies of the 1T'-phase: In a similar vein, to understand the phase transformation shown in the previous section in more detail, we have analyzed energetics between the vacancy line and 1T'-phase (cf. Fig. 7 (a)). The results in Fig. 7 (b) suggest that the formation energy per missing Te atom for single vacancy lines are lower than for the trapezoidal 1T'-phase, although the difference in the formation energies per Te atom between the single vacancy line and the local 1T'-phase is getting smaller with the increasing length of the vacancy line. The transformation effect has been observed more often in longer line defects, thus supporting our calculations.

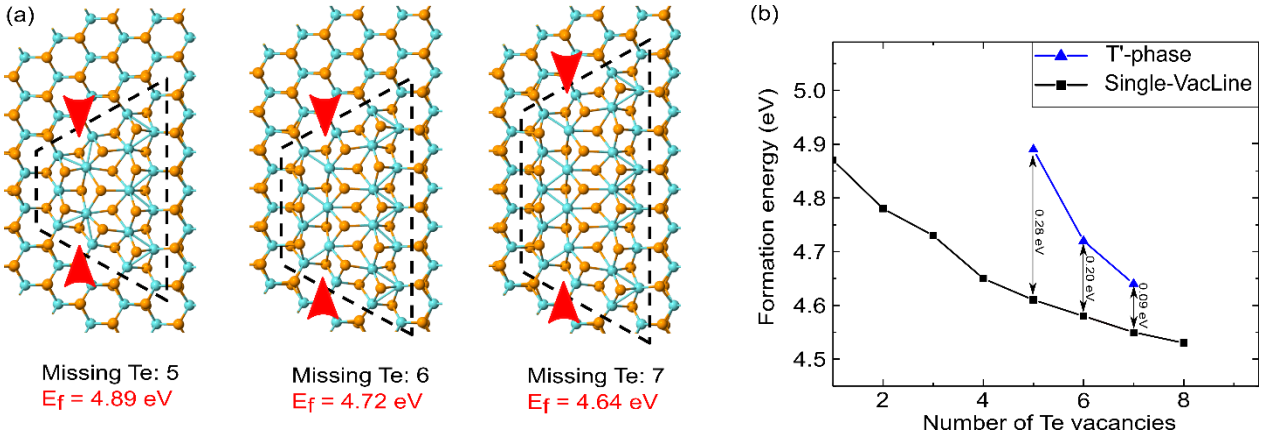

Figure 7: Modeled 1T'-phase islands of different sizes within the 1H matrix is shown in (a). Corresponding formation energies, given below the structure simulations, indicate that increasing the size of the 1T' islands results in lower formation energy per Te vacancy. (b) Formation energies of single-vacancy lines (black) and 1T'-phase (blue) for different vacancy lines.

Although single Te vacancy lines are formed under the electron beam and should be energetically more stable than the trapezoidal 1T'-phase island, the transformation is often observed, and the structure is remarkably stable under the irradiation with energetic electrons. We propose the 1T'-phase may again be stabilized by strain. The calculated lattice constants are a = b = 3.54 Å for the 1H-phase and a = 3.48 Å and b = 7.23 Å for the 1T'-phase. Embedding a 1T'-phase region within

an unstrained 1H-phase matrix thus means that the 1T'-phase region is tensile strained along a and compressively strained along b. Consequently, the tensile strain of the sample along b increasingly favors 1T'-phase over 1H-phase. Our calculations presented in Fig. 8 show that more than 6 % uniaxial strain along b-direction is necessary for the phase transformation of the pristine 1H to the 1T'-phase. This is a rather high value, but we stress that we considered purely uniaxial strain at zero temperature and without zero-point vibrations, while simulations[18] indicate that other components of strain and finite temperatures substantially reduce the critical strain value. Moreover, the results depend on the choice of the computational approach and specifically the choice of the exchange-correlation functional: for example, calculations using the hybrid Hartree–Fock/DFT method with the HSE functional[18] give lower stress values than the PBE/DFT approach we used. Besides, impurities and entropic contributions to the free energy at finite temperatures can also play an important role facilitating the transion to the T-pahse [DOI: 10.1021/acs.jpclett.7b01177]. While we know that vacancies induce tensile strain, a precise value is difficult to estimate.

However, our data in Fig. 8 also indicates that the introduction of Te vacancies lowers the required strain for a phase transformation in 1H-$MoTe_2$. Based on these results and assuming that the migration barriers shown in Fig. 3(g) are not dramatically increased by the presence of small tensile strain, the strain and the presence of Te vacancies result in a phase transformation that is further facilitated by electron beam-induced bond breaking.

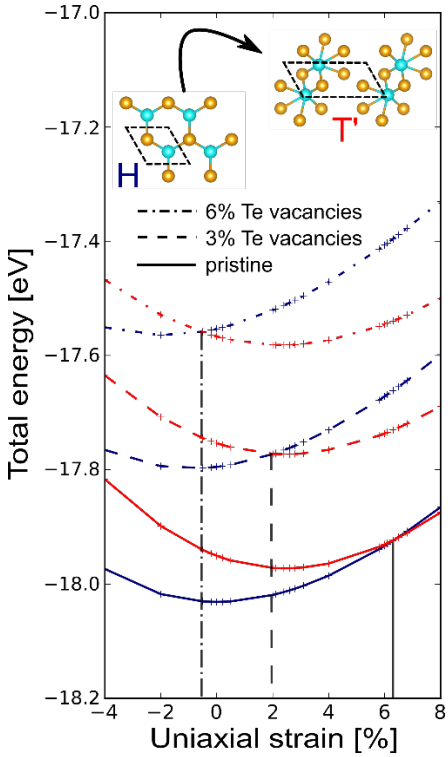

Figure 8: Calculated energies of the 1H (blue) and 1T'-phase (red) for various vacancy concentrations as functions of uniaxial strain along b-direction. The indicated strain refers to the 1H-phase, and the same value is also used in the 1T'-phase. Vertical lines indicate the cross-over points.

IV. Conclusions

Using 40 kV Cc/Cs-corrected HRTEM experiments on 1H-$MoTe_2$, we followed atom by atom the migration and agglomeration of single Te vacancies. We addressed open questions related to their transformation pathways to complex defect structures such as single Te vacancy lines and small islands of the 1T'-phase. Experimental data combined with the results of DFT calculations revealed: (i) All migrations of vacancies and extended defect structures can be deconstructed to two paths of motion of single Te atoms through the hexagonal crystal lattice. This step-by-step process leads to an even lower energy barrier for the movement of single Te vacancy lines than for individual single Te vacancies. The observed elementary migration events of the defect structures

are likely further accelerated by the energy transfer from the electron beam. (ii) The apparent changes in the preferred orientation of the line defects and stability of 1T'-phase regions are related to the development of strain in the sample, induced by the formation of vacancies, that are the atoms sputtered by the electron beam.

As evident from our results, energetic electrons provide the possibility to create defects and modify their density and in general the arrangement of atoms in atomically thin $MoTe_2$. Our findings should enhance the control over defects and better understand their transformations under electron beam and mechanical strain, potentially opening new pathways for defect-based engineering devices such as single-photon emitters, quantum dots, and metallic vacancy lines embedded into semiconducting 2D material. We note that mechanical strain can come not only from the defects, but also be created externally. A synergetic can be experimentally achieved by combining TEM with a scanning tunneling microscope (STM) or atom force microscope (AFM) located inside the TEM chamber. Such systems have been used to, e.g., assess the effects of defects on the mechanical properties of carbon nanotubes [DOI: 10.1021/acs.nanolett.6b02287] or study the edges in graphene sheets [DOI: 10.1021/acs.nanolett.9b04524]. On a larger scale (but without in-situ control of defects), defects cam be produced by ion irradiation, and then strain can be applied by bending the substrate or again, using AFM.

V. Acknowledgement:

We acknowledge funding from the German Research Foundation (DFG), project KR 48661/1, and through the collaborative research center "Chemistry of Synthetic 2D Materials" SFB-1415-417590517. We acknowledge the German Research Foundation (DFG) and the Ministry of Science, Researchand the Arts (M.W.K.) of the federal state of Baden-Württemberg, Germany, in

the frame of the SALVE (Sub Angström Low-Voltage Electron Microscopy) project (KA1295/21-1). The further, thank HLRS, Stuttgart, Germany, and TU Dresden (Taurus cluster) for generous grants of CPU time.

VI. References:

1. Chhowalla, M., Chhowalla, M., Shin, H. S., Eda, G., Li, L. J., Loh, K. P., & Zhang, H.. The chemistry of two-dimensional layered transition metal dichalcogenide nanosheets. *Nat. Chem.* **2013**, 5 (4), 263–275.
2. He, Y.-M., He, Y. M., Clark, G., Schaibley, J. R., He, Y., Chen, M. C., Wei, Y. J., Ding, X., Zhang, Q., Yao, W. Xu, X., et al. Single quantum emitters in monolayer semiconductors. *Nat. Nanotechnol.* **2015**, 10 (6), 497-502.
3. Tran, T. T., Tran, T. T., Wang, D., Xu, Z. Q., Yang, A., Toth, M., Odom, T. W., & Aharonovich, I. Deterministic coupling of quantum emitters in 2D materials to plasmonic nanocavity arrays. *Nano Lett.* **2017**, 17 (4), 2634–2639.
4. Klinovaja, J. & Loss, D. Spintronics in MoS_2 monolayer quantum wires. *Phys. Rev. B* **2013**, 88 (7), 75404.
5. Deng, K., Wan, G., Deng, P., Zhang, K., Ding, S., Wang, E., Yan, M., Huang, H. Zhang, H., Xu, Z., et al.. Experimental observation of topological Fermi arcs in type-II Weyl semimetal $MoTe_2$. *Nat. Phys.* **2016**, 12 (12), 1105–1110.
6. Han, G. H., Keum, D. H., Zhao, J., Shin, B. G., Song, S., Bae, J. J., Lee, J. Kim, J. H., Kim, H., Moon, B. H., *et al.* Absorption dichroism of monolayer 1T'-$MoTe_2$ in visible range. *2D Mater.* **2016**, 3 (3), 031010.
7. Mandyam, S. V, Kim, H. M. & Drndić, M. Large area few-layer TMD film growths and their applications. *J. Phys. Mater.* **2020**, 3 (2), 024008.
8. Novoselov, K. S., Geim, A. K., Morozov, S. V., Jiang, D., Zhang, Y., Dubonos, S. V., Grigorieva I. V. and Firsov A. A. Electric Field Effect in Atomically Thin Carbon Films. *science* **2016**, 306 (5696), 666–669.
9. Oostinga, J. B., Heersche, H. B., Liu, X., Morpurgo, A. F. & Vandersypen, L. M. K. Gate-induced insulating state in bilayer graphene devices. *Nat. Mater.* **2008**, 7 (2), 151–157.
10. Grigorenko, A. N., Polini, M. & Novoselov, K. S. Graphene plasmonics. *Nat. Photonics* **2012**, 6 (11), 749–758.
11. Warner, J. H., Rümmeli, M. H., Ge, L., Gemming, T., Montanari, B., Harrison, N. M., Büchner, *B. &* Briggs, G. A. D. Structural transformations in graphene studied with high spatial and temporal resolution. *Nat. Nanotechnol.* **2009**, 4 (8), 500–504.

12. Watanabe, K., Taniguchi, T. & Kanda, H. Direct-bandgap properties and evidence for ultraviolet lasing of hexagonal boron nitride single crystal. *Nat. Mater.* **2004**, 3 (6), 404–409.
13. Pizzochero, M. & Yazyev, O. V. Point defects in the 1T′ and 2H phases of single-layer MoS_2: A comparative first-principles study. *Phys. Rev. B* **2017**, 96 (24), 245402.
14. Krishnamoorthy, A., Bassman, L., Kalia, R. K., Nakano, A., Shimojo, F., & Vashishta, P. Semiconductor-metal structural phase transformation in $MoTe_2$ monolayers by electronic excitation. *Nanoscale* **2018**, 10 (6), 2742–2747.
15. Lehnert, T., Lehtinen, O., Algara-Siller, G. & Kaiser, U. Electron radiation damage mechanisms in 2D $MoSe_2$. *Appl. Phys. Lett.* **2017**, 110 (3), 033106.
16. Li, Y., Duerloo, K. A. N., Wauson, K. & Reed, E. J. Structural semiconductor-to-semimetal phase transition in two-dimensional materials induced by electrostatic gating. *Nat. Commun.* **2016**, 7 (1), 10671.
17. Berry, J., Zhou, S., Han, J., Srolovitz, D. J. & Haataja, M. P. Dynamic phase engineering of bendable transition metal dichalcogenide monolayers. *Nano Lett.* **2017**, 17 (4), 2473–2481.
18. Duerloo, K. A. N., Li, Y. & Reed, E. J. Structural phase transitions in two-dimensional Mo- and W-dichalcogenide monolayers. *Nat. Commun.* **2014**, 5 (1), 4214.
19. Brown, B. E. The crystal structures of WTe_2 and high-temperature $MoTe_2$. *Acta Crystallogr.* **1966**, 20 (2), 268–274.
20. Cho, S., Kim, S., Kim, J. H., Zhao, J., Seok, J., Keum, D. H., Baik, J., Choe, D.-H., Chang, K. J., Suenaga, K. et al. Phase patterning for ohmic homojunction contact in $MoTe_2$. *Science.* **2015**, 349 (6248), 625–628.
21. Wang, Y., Xiao, J., Zhu, H., Li, Y., Alsaid, Y., Fong, K. Y., Zhou, Y., Wang, S., Shi, W., Wang, Y., *et al.* Structural phase transition in monolayer $MoTe_2$ driven by electrostatic doping. *Nature* **2017**, 550 (7677), 487–491.
22. Zhou, Y. & Reed, E. J. Structural Phase Stability Control of Monolayer $MoTe_2$ with Adsorbed Atoms and Molecules. *J. Phys. Chem. C* **2015**, 119 (37), 21674–21680.
23. Komsa, H. P., Kotakoski, J., Kurasch, S., Lehtinen, O., Kaiser, U., & Krasheninnikov, A. V. Two-dimensional transition metal dichalcogenides under electron irradiation: Defect production and doping. *Phys. Rev. Lett.* **2012**, 109 (3), 035503.
24. KC, S., Longo, R. C., Addou, R., Wallace, R. M. & Cho, K. Impact of intrinsic atomic defects on the electronic structure of MoS2 monolayers. *Nanotechnology* **2014**, 25 (37), 375703.
25. Egerton, R. F., Li, P. & Malac, M. Radiation damage in the TEM and SEM. *Micron* **2004**, 35 (6), 399–409.
26. Lin, Z., Carvalho, B. R., Kahn, E., Lv, R., Rao, R. & Terrones, H., Defect engineering of two-dimensional transition metal dichalcogenides. *2D Mater.* **2016**, 3 (2), 022002.

27. Barja, S., Wickenburg, S., Liu, Z. F., Zhang, Y., Ryu, H., Ugeda, M. M., Hussain, Z., Shen, Z.-X., Mo, S.-K., Wong, E., *et al.* Charge density wave order in 1D mirror twin boundaries of single-layer $MoSe_2$. *Nat. Phys.* **2016**, 12 (8), 751–756.
28. Guguchia, Z., Kerelsky, A., Edelberg, D., Banerjee, S., von Rohr, F., Scullion, D., Augustin, M., Scully, M., Rhodes, D. A., Shermadini, Z., *et al.* Magnetism in semiconducting molybdenum dichalcogenides. *Sci. Adv.* **2018**, 4 (12), eaat3672.
29. Lehnert, T., Ghorbani-Asl, M., Köster, J., Lee, Z., Krasheninnikov, A. V., & Kaiser, U. Electron-Beam-Driven Structure Evolution of Single-Layer $MoTe_2$ for Quantum Devices. *ACS Appl. Nano Mater.* **2019**, 2 (5), 3262–3270.
30. Elibol, K., Susi, T., Argentero, G., Reza Ahmadpour Monazam, M., Pennycook, T. J., Meyer, J. C., & Kotakoski, J. Atomic Structure of Intrinsic and Electron-Irradiation-Induced Defects in $MoTe_2$. *Chem. Mater.* **2018**, 30 (4), 1230–1238.
31. Komsa, H. P., Kurasch, S., Lehtinen, O., Kaiser, U. & Krasheninnikov, A. V. From point to extended defects in two-dimensional MoS_2: Evolution of atomic structure under electron irradiation. *Phys. Rev. B - Condens. Matter Mater. Phys.* **2013**, 88 (3), 035301.
32. Vellinga, M. B., de Jonge, R. & Haas, C. Semiconductor to metal transition in $MoTe_2$. *J. Solid State Chem.* **1970**, 2 (2), 299–302.
33. Lee, C. W. & Schleife, A. Hot-Electron-Mediated Ion Diffusion in Semiconductors for Ion-Beam Nanostructuring. *Nano Lett.* **2019**, 19 (6), 3939–3947.
34. Kretschmer, S., Lehnert, T., Kaiser, U. & Krasheninnikov, A. V. Formation of defects in two-dimensional MoS_2 in the transmission electron microscope at electron energies below the knock-on threshold: the role of electronic excitations. *Nano Lett.* **2020**, 20 (4), 2865–2870.
35. Sensoy, M. G., Vinichenko, D., Chen, W., Friend, C. M. & Kaxiras, E. Strain effects on the behavior of isolated and paired sulfur vacancy defects in monolayer MoS_2. *Phys. Rev. B* **2017**, 95 (1), 014106.
36. Benameur, M. M., Radisavljevic, B., Héron, J. S., Sahoo, S., Berger, H., & Kis, A. Visibility of dichalcogenide nanolayers. *Nanotechnology* **2011**, 22 (12), 125706.
37. Blake, P., Hill, E. W., Castro Neto, A. H., Novoselov, K. S., Jiang, D., Yang, R., Booth, T. J. & Geim, A. K. Making graphene visible. *Appl. Phys. Lett.* **2007**, 91 (6), 063124.
38. Beal, A. R. & Hughes, H. P. Kramers-Kronig analysis of the reflectivity spectra of 2H-MoS_2, 2H-$MoSe_2$ and 2H-$MoTe_2$. *J. Phys. C Solid State Phys.* **1979**, 12 (5), 881–890.

TOC Graphic:

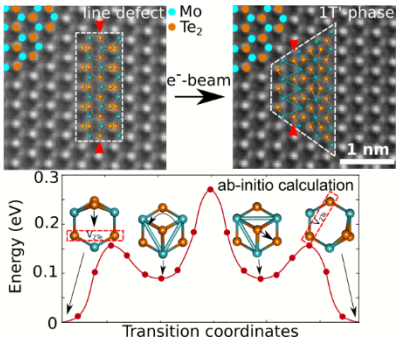
line defect
Mo
Te2
e⁻-beam
1T' phase
1 nm
ab-initio calculation
Energy (eV)
0.3
0.2
0.1
0
Transition coordinates